Lithuanian Journal of Physics, Vol. **54**, No. 3, pp. 187–198 (2014)

PHOTOLUMINESCENCE FEATURES AND CARRIER DYNAMICS IN InGaN HETEROSTRUCTURES WITH WIDE STAIRCASE INTERLAYERS AND DIFFERENTLY SHAPED QUANTUM WELLS

A. Kadys, T. Malinauskas, M. Dmukauskas, I. Reklaitis, K. Nomeika, V. Gudelis,

R. Aleksiejūnas, P. Ščajev, S. Nargelas, S. Miasojedovas, and K. Jarašiūnas

Institute of Applied Research, Vilnius University, Saulėtekio 9-III, LT-10222 Vilnius, Lithuania
E-mail: kestutis.jarasiunas@ff.vu.lt

Received 22 April 2014; revised 15 June 2014; accepted 23 September 2014

We present a comprehensive study of photoexcited carrier dynamics in differently grown InGaN/InGaN multiple quantum well (MQW) structures, modified by insertion of a wide interlayer structure and subsequent growth of differently shaped quantum wells (rectangular, triangular, trapezoidal). This approach of strain management allowed the reduction of dislocation density due to gradually increasing In content in the interlayer and shaping the smooth quantum well/barrier interfaces. A set of c-oriented MQW structures emitting at 470 nm were grown at Vilnius University, Institute of Applied Research, using a closed coupled showerhead type MOCVD reactor. Photoluminescence (PL) spectra of MQW structures were analysed combining continuous wave and pulsed PL measurements. Reactive ion etching of the structures enabled discrimination of PL signals originated in the InGaN interlayer structure, underlying quantum wells, and quantum barriers, thus providing growth-related conditions for enhanced carrier localization in the wells. Time-resolved PL and differential transmission kinetics provided carrier lifetimes and their spectral distribution, being the longest in triangular-shape QWs which exhibited the highest PL intensity. The light-induced transient grating (LITG) technique was used to determine the spatially averaged carrier lifetime in the entire heterostructure, in this way unravelling the electronic quality of the LED internal structure at conditions similar to device performance. LITG decay rates at low and high excitation energy densities revealed increasing with photoexcitation nonradiative recombination rate in the triangular and trapezoidal wells.

Keywords: light emitting diodes, nitride semiconductors, photoluminescence, carrier recombination

PACS: 73.21.Fg; 78.67.-n; 78.47.-p

1. Introduction

Despite extensive research efforts for a decade, the physical origin of the dominant mechanism of emission efficiency droop in InGaN light emitting diodes (LEDs) has not been clarified. Physical mechanisms which may lead to droop at high injection levels are reviewed and classified [1–3]. They discriminate internal mechanisms of nonradiative losses in the active region of a LED and those caused by the carrier leakage. The former case deals with a problem why all carriers injected into the active region are not consumed by radiative recombination and what are the nonradiative recombination pathways that contribute at high injections (e. g. Auger recombination in the InGaN wells was invoked [3, 4]). It was also suggested that additional nonradiative losses may appear at high injections due to carrier delocalization from the states within the potential minima where they recombine radiatively at low injections. The delocalized carriers are mobile and can occupy the extended states as well as diffuse to the defect sites and recombine nonradiatvely (a hypothesis of defect-activated nonradiative recombination was proposed by Hader [5] and verified experimentally in violet and blue LEDs [6, 7]). Saturation of a radiative recombination rate cannot be excluded as well [8].

Other processes deal with nonradiative losses outside the active region, and they may have a number of forms leading to enhanced droop. The electron leakage in a biased device can be promoted by the carrier spillover above the barriers, while experimental data have shown that the effect is not large enough to singlehandedly explain the efficiency droop [9]. Besides that, electron overshooting has been suggested as the dominant mechanism [2, 10]. Here, the electrons injected from the n-GaN layer into the well gain high kinetic

energy and become hot; therefore, only a part of them can contribute to radiative (or nonradiative) recombination in the active layer. The rest of the electrons can cross the active region and reach the p-GaN layer by ballistic transport. Correspondingly, several technological modifications to the GaN LED structure have been proposed as droop remedies of the later effect. It has been shown that insertion of a few rather thick InGaN layers with increasing In content (the so-called InGaN staircase electron injector, SEI) provides conditions for electron thermalization before they reach the active region [10]. Other technological approaches include variation of the thickness, the number, and the shape of QWs, engineering the quantum barriers, insertion of the electron blocking layer, or growth of the wells along semi- and non-polar orientations [1].

We note that up to now an impact of the SEI structure on emission efficiency was revealed by measuring electroluminescence and external quantum efficiency (EQE) dependence in a biased LED structure. Despite some previous reports that the droop of internal quantum efficiency (IQE) was not observed under optical carrier generation at rates comparable to those under electrical injection [11], a clear correlation of the EQE onset with saturation of IQE gives strong evidence that the QW properties strongly contribute to the photo- and electroluminescence efficiency. Therefore, investigation of photoexcited carrier dynamics in the entire LED structure (including SEI layers) needs further studies to determine the InGaN alloy related radiative and nonradiative recombination rates.

In this work we present several technological modifications of the active LED region and subsequent comprehensive analysis of it by means of various optical techniques. To reduce dislocation density, strain relaxation management was realized by inserting thick InGaN layers with gradually increasing In content as well growing the smooth quantum well/barrier interfaces (instead of abrupt change of In content). Therefore, a SEI structure with gradual increase of In density was grown on the n-GaN template layer before the growth of a QW structure. Secondly, shaping of the spatial profile of the wells is supposed to improve shape-dependent overlap of electron-hole wave functions and enhance the radiative emission efficiency [12, 13]. For evaluation of the LED active region quality, the structural and optical properties of the grown heterostructures were analysed using X-ray diffraction (XRD) and atomic force microscopy (AFM) data, PL spectra at low continuous wave (CW) injections as well as at higher photoexcitations by using picosecond and femtosecond pulses, also investigating carrier dynamics. For the latter goal, carrier recombination pathways in the structures were investigated by applying various time-resolved techniques: photoluminescence spectroscopy (PL), differential transmission (DT), and light-induced transient gratings (LITG). These techniques allowed us to investigate PL spectra and spectral distribution of the carrier recombination rate, discriminate growth-dependent contribution of SEI or QW to the entire PL spectrum, verify the higher quantum efficiency in non-rectangular quantum wells, and evaluate the electronic quality of the entire heterostructure at conditions similar to device performance.

2. Samples and techniques

The MQW structures were grown using an *AIXTRON* CCS (closed coupled showerhead) MOCVD reactor at Vilnius University. Trimetilindium (TMI), trimetilgalium (TMG), and ammonia were used as precursors for In, Ga, and N, accordingly. An undoped ~3 μm thick GaN layer (see Fig. 1) was deposited on a sapphire substrate with the c (0001) crystallographic

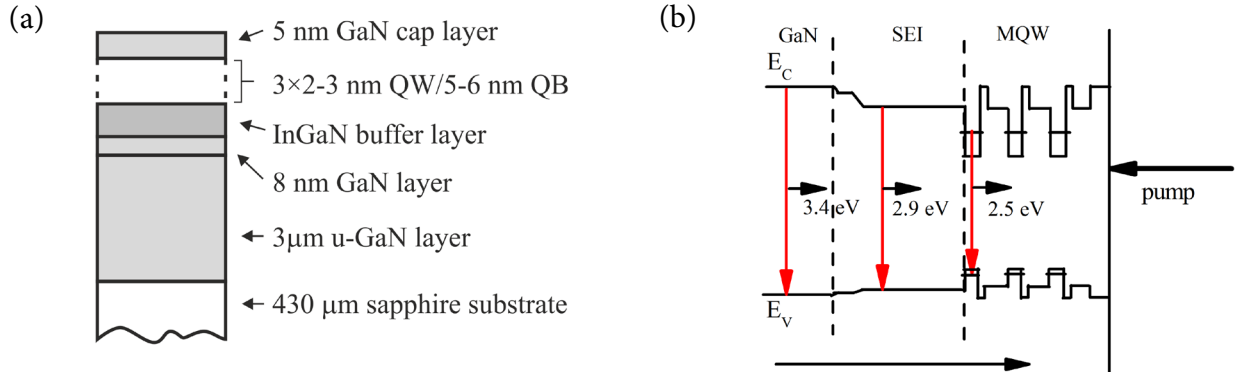

Fig. 1. (a) Scheme of the grown heterostructure. (b) Profiles of conduction E_C and valence E_V band edges in the absence of polarization fields, obtained using $In_xGa_{1-x}N$ band-gap dependence on In concentration E_G (eV) = 3.4(1–x) + 0.7 x – bx(1–x) with the bowing parameter b = 2.5 eV [20] and the valence band offset ΔE_V(eV) = 0.7x.

orientation, tilted by 0.25–0.35 degree with respect to the m-plane. The sapphire substrate was initially decontaminated at 1800 °C, then its surface was nitridized, and a thin (20–5 nm) amorphic GaN layer was grown at 530 °C. During the next step, the temperature was raised to 1070 °C leading to the crystallization of the layer, which then was used to deposit a 3.5 μm thick crystalline GaN buffer layer. It had an electron density of $n_e \approx 10^{17}$ cm^{-3} and electron mobility μ_e ~200 cm^2/Vs.

A wide InGaN buffer layer, or the so-called SEI structure, was grown on the GaN layer before deposition of a LED active region, composed of three quantum wells and three barriers. The SEI structure consisted of three layers (see Fig. 2(a)) – a 2 nm thick layer with low indium content grown at 950 °C, a 5–6 nm thick In layer with gradually increasing In content, and the final 90 nm thick InGaN layer grown at 800 °C with the highest In content (4–11% of In as determined by XRD). A rather thick interlayer was chosen to obtain fully relaxed and less defective InGaN layers, taking into account that critical thickness of $In_xGa_{1-x}N$ on GaN for x in the range from 5% to 15% is around 50 nm [14, 15]. The In content in the layers was changed by varying growth temperature as the TMI/TMG = 1.5 ratio was kept constant.

The QWs were grown at around 700 °C to reach high In content (up to ~25%). Three periods of 2–3 nm thick wells and ~6 nm barriers were grown. After each QW, a protective 1 nm thick GaN layer was deposited at 700 °C to prevent the In evaporation from the QW during the temperature ramp-up for barrier growth. The In concentration profile of QWs in A, B, and C structures was nominally rectangular, as the growth temperature was kept constant during the well growth to get constant In concentration. On the other hand, the D and E structures were grown by ramping temperatures during the well growth that led to the triangular (D) or trapezoidal (E) In concentration and band-gap profile in QWs. The gradient increase of In at the interfaces allowed to accommodate stress and avoid generation of additional structural defects in the wells. The intended structure, growth temperatures, and thicknesses are shown in Fig. 2(a). On the top of each active structure a 5 nm thick GaN cap layer was deposited. QW and barrier thicknesses were estimated from XRD $\omega/2\theta$ scans using (0002) reflection (Fig. 2(b)). We note that a reference $In_xGa_{1-x}N$ MQW structure (sample F, not shown in Fig. 2(a); the wells are the same as in the sample A) was also grown directly on the GaN template without the SEI interlayer under the same growth conditions.

A number of techniques were used for optical characterization of the LED structures. A standard set-up of time-integrated PL spectroscopy was employed using ~355 nm excitation pulses from a picosecond YAG:Nd^{3+} laser and detecting the PL spectra by a thermoelectrically cooled *Princeton Instruments* CCD camera. For low excitation CW PL measurements, a fluorimeter LS–55 was used, where samples were excited at 380 nm. For time-resolved PL

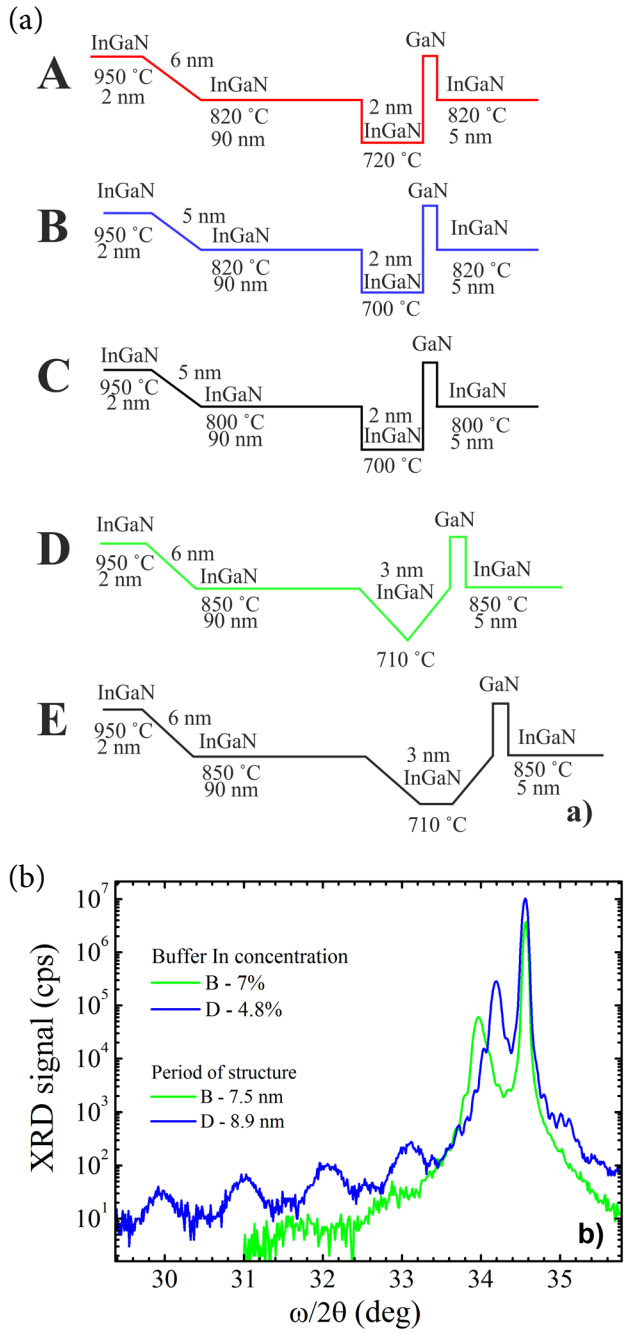

Fig. 2. (a) Band-gap profile with the corresponding growth algorithm in the investigated structures; for simplicity, only the first quantum well and quantum barrier is shown in the drawing. A, B, and C are the structures with rectangular shape, while D and E with triangular and trapezoidal shape of quantum wells. (b) XRD $\omega/2\theta$ scan data in samples B and D.

measurements, a picosecond YAG:Nd^{3+} laser (emitting at 355 nm and water Raman-shifted 405 nm wavelengths) was combined with an *Hamamatsu* C10627 streak camera and Acton SP2300 monochromator, providing the temporal resolution of 20 ps.

The experimental set-up for spectrally and time-resolved DT was based on a commercial Ti:Sapphire femtosecond laser (Spitfire, *Spectra Physics*) delivering 800 nm pulses of 120 fs duration at a 1 kHz repetition rate (Fig. 3(a)). The output of the laser was split into two equal parts. One was used to pump the optical parametric amplifier (TOPAS, *Light Conversion*) providing 120 fs pulses at wavelengths continuously tunable between 1200–2500 nm. The pump was set to 400 nm (3.1 eV) and absorbed in the QWs and SEI, avoiding carrier photogeneration in the GaN buffer layer. The second beam was delayed and focused on a CaF_2 window generating a short pulse of white light. This spectrally broad pulse (330–700 nm) was used to probe changes in absorption spectra at various times after the photoexcitation. The differential transmission spectrum is presented as instantaneous optical density $OD(\lambda,t) = \log(T_0(\lambda)/T(\lambda,t))$; where $T_0(\lambda)$ and $T(\lambda,t)$ stand for the sample transmittance spectrum without and with the pump pulse at a time instant t. In this way, DT technique provided means to observe evolution of state occupancy in InGaN QWs with high temporal and spectral resolution.

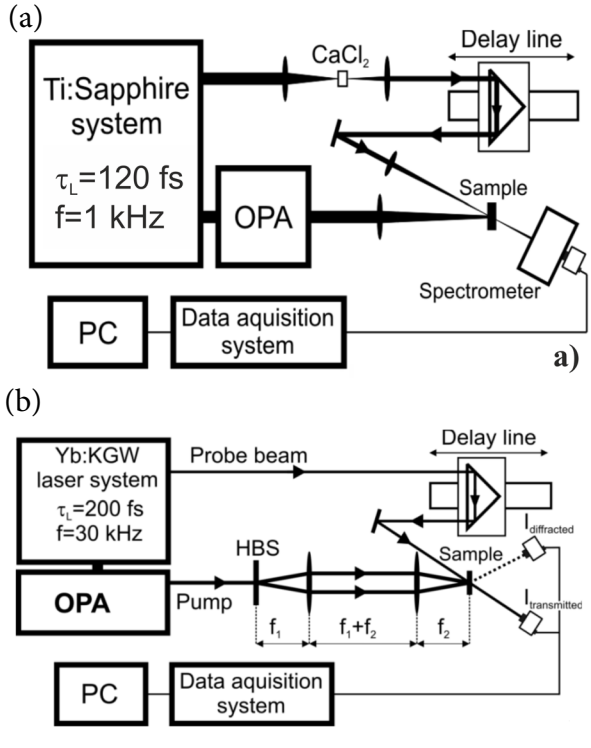

Fig. 3. Experimental set-ups of (a) DT and (b) LITG techniques.

Unlike the conventional pump-probe set-up, where samples are excited by the Gaussian-like spatial profile, LITG technique for photoexcitation uses the interference field of two coherent beams [16] (Fig. 3(b)). This results in recording of a free-carrier grating with period Λ and carrier density spatial modulation ΔN_0, the decay of which can be probed by diffraction of a delayed probe beam, providing an instantaneous diffraction efficiency $\eta(t) \sim \Delta N_0^2 \exp(-2t/\tau_G)$. The grating decay time τ_G at different grating periods allows determination of the carrier diffusion coefficient D and the carrier lifetime τ_R according to the $1/\tau_G = 1/\tau_R + 4\pi^2 D/\Lambda^2$ relationship. Such an approach has several advantages, one of which being the ability to measure the time evolution of the overall free carrier density.

3. Results and discussion

3.1. Sample morphology and structural quality

The structural quality and surface morphology of the grown structures was evaluated by scanning electron microscopy (SEM, Fig. 4) and atomic force microscopy (AFM, Fig. 5). SEM and AFM images showed that samples D and E with the triangular and trapezoidal wells, correspondingly, have the significantly smoother surfaces. The surface roughness measured by AFM decreased down to around 3 nm in D and E samples with respect to the rectangular ones with the roughness of 7 nm. Also, the AFM scans showed that the dislocation density (dark spots) was lower by a factor of 2 in the graded quantum wells (samples D and E) if compared to the reference sample with the constant In concentration (the dark spot density was 5×10^8 cm^{-2} (sample A) and $2–3 \times 10^8$ cm^{-2} (samples D and E). Also, the observed hexagons were much larger in the samples D and E.

3.2. PL emission at steady state conditions: PL spectra

In order to optimize the growth parameters, continuous wave (CW) PL spectra were recorded and PL output at the QW peak position (~470 nm) was compared between the variously grown structures (Fig. 6). The weaker additional bands appearing at ~370 and 400 nm were attributed to GaN buffer and interlayer emission, correspondingly, and will be addressed in the later section.

Among the rectangular QWs grown at different temperatures, the most intensive PL output at 470 nm was found in structure A (Fig. 6(a)). Therefore, the lower growth temperature of ~720 °C was assumed as a more suitable one for growth of the rectangular QWs. Then the PL efficiency was maximized by varying the well shape, and the highest PL signal was

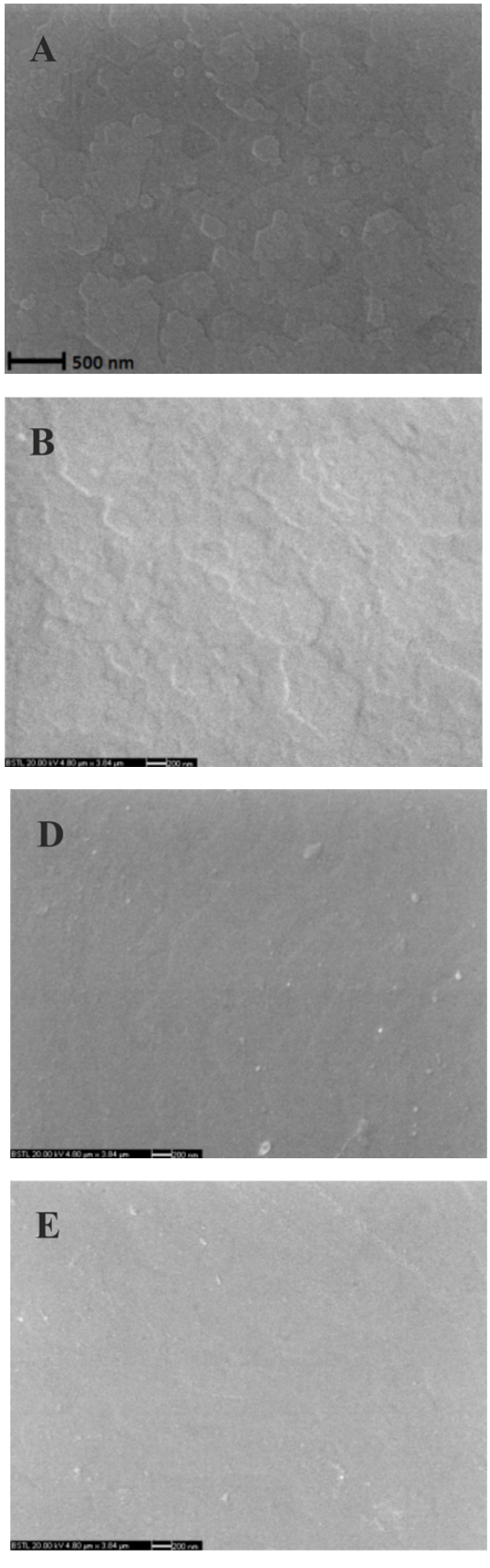

Fig. 4. SEM surface images of samples A, B, D, and E taken at the same magnification ratio. The surface roughness in samples A and B is noticeably larger than that in samples D and E.

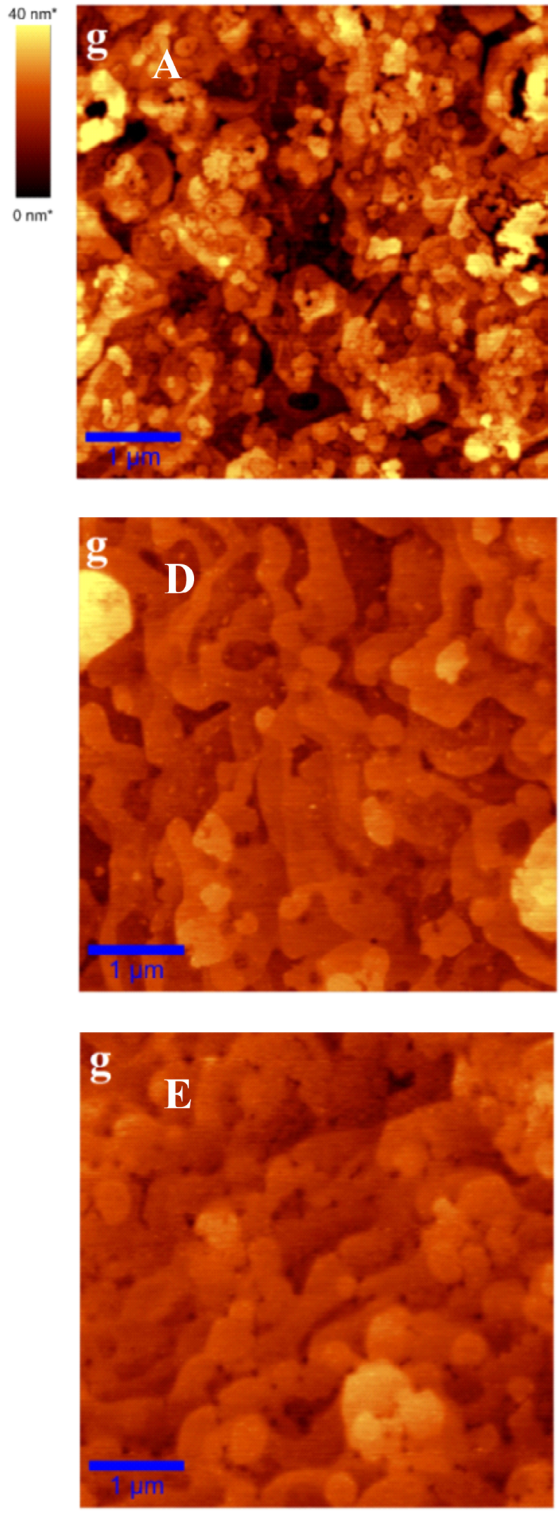

Fig. 5. AFM scans of samples A, D, and E.

obtained for the triangular QWs (sample D in Fig. 6(b)). This can be explained by better In incorporation and its weaker segregation due to continuous change of strain [12, 13]. Also, it has been shown that the e-h wave function overlap is better in the triangular and trapezoidal QWs [12, 13].

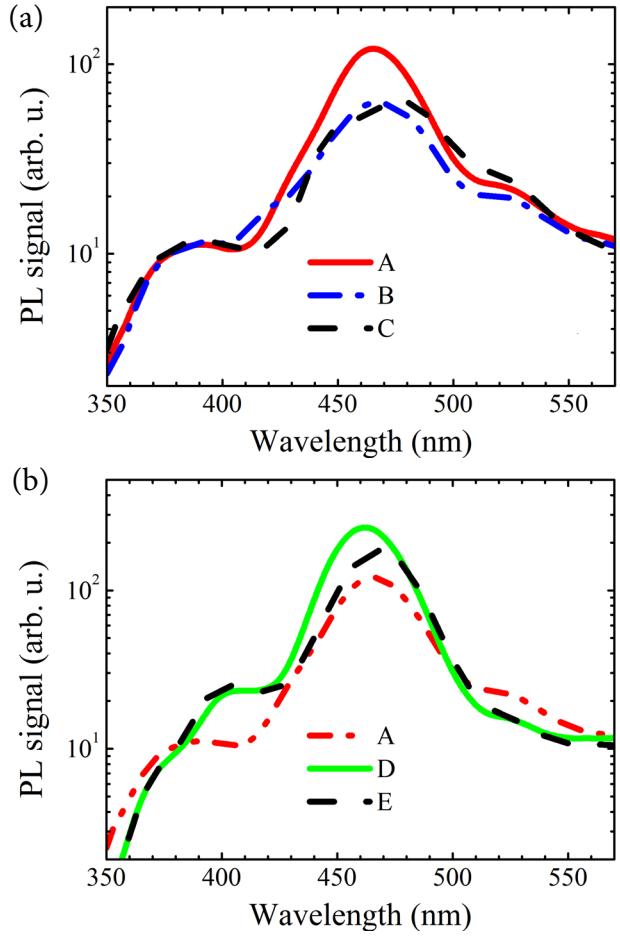

Fig. 6. Comparison of CW photoluminescence spectra in the structures with the rectangular QWs grown at various temperatures (a) and for differently shaped wells (b). For growth conditions, see Fig. 2(a). The used excitation power density was 20 μW/cm^2 at 380 nm.

3.3. PL characteristics at pulsed excitation

To get a deeper insight into PL features at higher free carrier densities, PL measurements were performed under pulsed 355 nm excitation (Fig. 7). Three distinct peaks were identified in the PL spectra. A wide peak at 450–470 nm saturating with excitation was attributed to the emission from the wells. The second stronger peak was blue-shifted with respect to QW emission. Its origin can be related to the emission from the thick SEI layer, since such a peak was absent in sample F without the SEI. In addition, variation of In content in the SEI leads to the shift of this peak position from 395 to 415 nm. The strongest SEI-related emission was observed in sample B at 420 nm (having the In concentration of about 7%, as the In content above 10% causes degradation of the InGaN epilayer and decrease of its PL intensity [6]). The third peak at 370 nm arises from the GaN barrier, as its position coincides with that from the bulk GaN [17].

To confirm the origin of the strong PL peaks in the 390–420 nm range, two steps of the reactive ion etching were performed on the LED structures, after which the PL spectra were measured again (see Fig. 8). Each step removed ~36 nm from the top of the structure. The first etching removed the 5 nm thick cap layer and the 25–30 nm thick QW structure (3 periods of QWs with barriers). The second etching removed a part of the SEI structure.

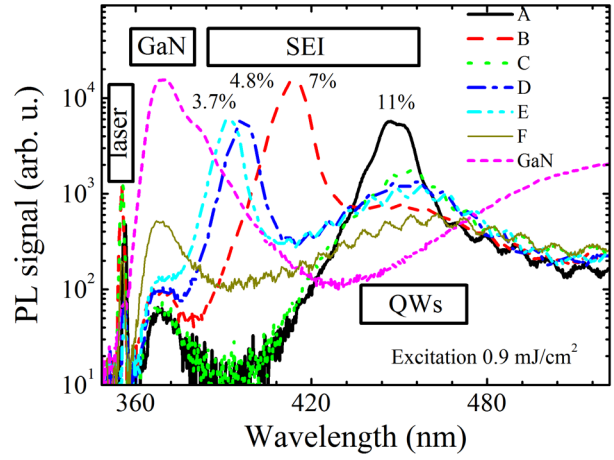

Fig. 7. Comparison of photoluminescence spectra in the studied samples using the picosecond pulses at 355 nm with energy density of I_0 = 0.9 mJ/cm^2. In content in the SEI layers is indicated in the figure. PL of bulk GaN shows the spectral position of the quantum barriers in the structures. The sample without the SEI (sample F) is also shown for comparison.

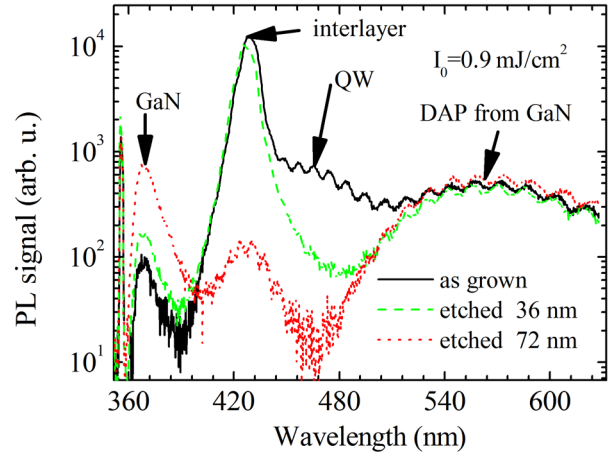

Fig. 8. PL spectra in the as-grown sample B (black line online), after the etching out the QWs (green line online), and the part of the SEI structure (red line online).

It was observed that after etching out the QWs the wide band at 470 nm almost disappeared, which proves that this band is caused by the emission from the wells. After the second etching step, the band at 420 nm also almost disappeared. The latter peak can be attributed to luminescence of the upper part of the InGaN SEI layer that has a better structural quality (critical depth for the InGaN alloy with 7% of In is expected to be 50 nm [14]). The lower part of SEI is believed to contain a high density of point defects and dislocations, which results in a weaker and broader PL spectrum [6, 18]. The emission at 370 nm from the GaN buffer increased after the etching due to reduced re-absorption by the InGaN layers. The 600 nm peak did not considerably change after the etching and was probably related to donor-acceptor pair (DAP) recombination in the GaN buffer (called yellow luminescence [19]).

The In composition in the wells can be estimated using the emission wavelengths and the well thickness. In all cases, QW emission peaks at ~470 nm (2.6 eV, Fig. 6) indicating the similar In content in all QWs. According to calibration, 25% of indium should be present in QWs grown at 710 ± 10 °C temperature. Relying on dependence of InGaN band-gap energy, it would provide 2.3 eV InGaN band-gap [20], whereas carrier confinement in the 3 nm thick well shifts up the lowest transition energy; therefore, PL occurs at 2.5 eV (estimation of the first electronic level position in the well according to $E_1 = h^2/(8m_e d^2)$ relationship [21] provided 0.22 eV shift). The large width (~240 meV) of the emission peak can be explained by thermal broadening, variations of QW thickness and In content in the wells.

The PL spectra dependence on excitation fluence is provided in Fig. 9. It was observed that PL peak intensities in both the GaN buffer and SEI interlayer continuously increase with the excitation, while the QW peak almost saturates. Fig. 10 shows the dependence of PL peak intensity versus excitation for various spectral regions of the grown structures. These dependences were fitted by power functions with the different indices that reflect carrier generation and recombination peculiarities. At high excitations, the sublinear dependence $I_{PL} \sim I_0^{0.4}$ for the QW emission points out the saturation of the PL signal, while the superlinear growth $I_{PL} \sim I_0^{1.4}$ is observed for the SEI interlayer.

In the QWs, PL intensity increases linearly at low excitations indicating the excitonic emission in QW band tails. At higher excitations, saturation of PL emission intensity from the wells can be explained by filling of the localized states (Fig. 10(a)). PL dependence in the interlayer exhibits much steeper dependence on excitation, which is typical of bulk GaN (slope of 2 corresponds to quadratic increase of PL signal with excitation, as the linear increase of electron-hole concentration, $N_{eh} \propto \alpha I_0$, leads to the bimolecular recombination, $I_{PL} \propto N_{eh}^2$). The decrease of the slope value at high injections (I_0>1 mJ/cm²) is a typical case for bulk semiconductors indicating interaction of various recombination mechanisms and saturation of the radiative recombination rate [8].

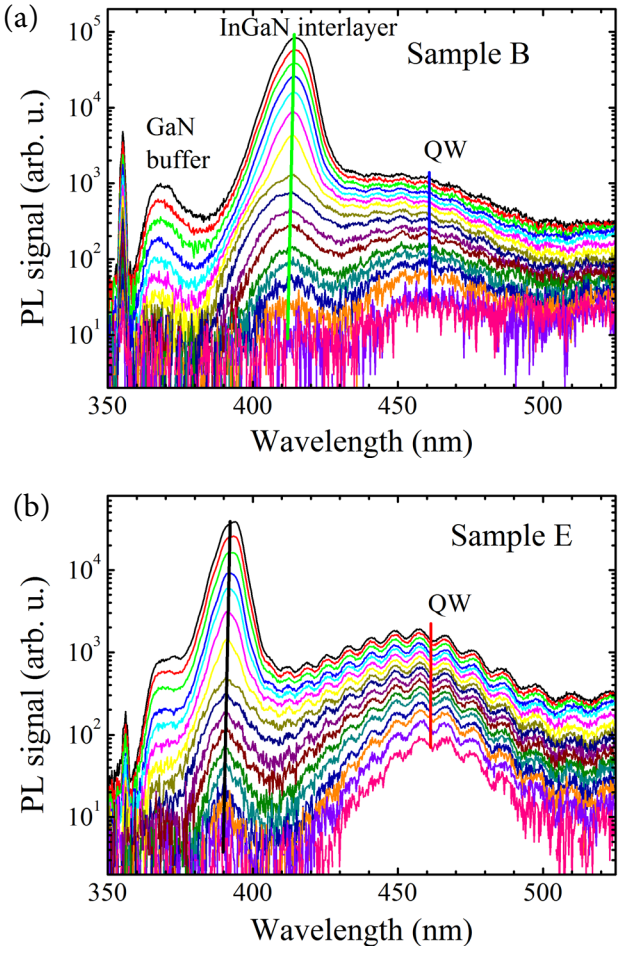

Fig. 9. PL spectra: (a) in the rectangular QW (sample B) and (b) in the trapezoidal QW (sample E) under the pulsed excitation at 355 nm.

It was observed that PL emission from the samples with profiled QWs (D and E samples, Fig. 10(a)) at pulsed excitation has the highest PL efficiency, thus confirming PL measurements under steady-state excitation conditions. In the latter structures, In concentration in the SEI interlayer is lower, thus favouring better carrier localization in QWs. In A and C samples, the QW spectral position overlaps with the SEI emission peak (Fig. 7), indicating weak localization in the wells; therefore, emission from the well and SEI cannot be separated, especially at high excitations (Fig. 10(b)). Consequently, too high concentration of In in the SEI layer leads to rather weak localization of carriers in the wells and rather weak emission from the wells. It is worth noting that the F sample exhibits only the QW

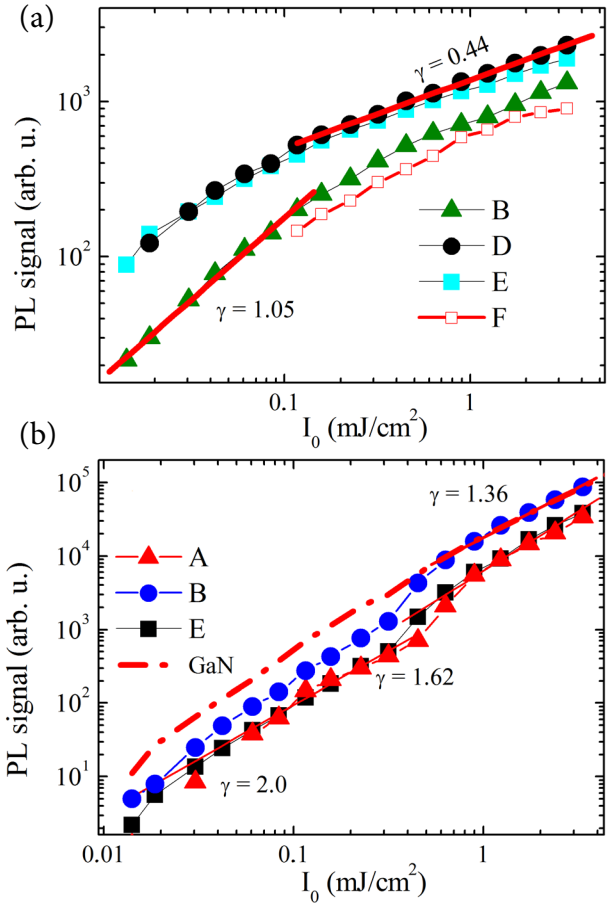

Fig. 10. PL intensity vs. excitation energy fluence at 355 nm for emission from the QWs at 470 nm (a) and from the SEI peaks (b). Saturation of PL ($\gamma = 0.44$, (a)) indicates filling of the localized states in the QWs; PL superlinear increase in (b) reveals its origin in the bipolar carrier recombination from the weakly localized states in the SEI.

peak, as there is no SEI interlayer. A comparison of PL signal from the rectangular wells F with respect to B (which has the SEI interlayer) points out to a positive impact of the interlayer, i. e. increase of the structural quality of the subsequently grown quantum wells.

The further PL measurements used selective photoexcitation of quantum wells at 405 nm; at this wavelength, the photon energy was sufficient to excite the quantum wells but not enough to excite the barriers and interlayers. This was confirmed by measurements of PL spectra at selective photoexcitation (Fig. 11(a)), and time-resolved PL kinetics provided carrier lifetimes in the differently shaped quantum wells (Fig. 11(b)).

It was observed that the blue-shift of PL appears due to screening of the quantum confinement Stark effect (QCSE) and filling of the localized states (Fig. 11(a)). Carrier lifetime of the sample D is ~4 times larger with respect to sample B, indicating the enhanced carrier localization in the former structure. Consequently, a few times longer lifetime provides ~3 times higher PL intensity (see Fig. 10(a)). Rather weak dependence of PL lifetime on excitation (at excitation above 0.1 mJ/cm^2) in D and E samples indicated the dominant channel of nonradiative recombination in the wells; here, a twice higher PL efficiency at 0.1 mJ/cm^2 with respect to 0.01 mJ/cm^2 excitation correlated with corresponding lifetime increase (from 0.2 to 0.4 ns) in sample D, indicating saturation of point defects [7]. A similar effect was also observed in sample E. A shorter carrier lifetime of 47 ps in sample F without SEI structure indicated a positive role of the SEI layer. We also note that at 355 nm excitation the PL decay time in the wells was also weakly dependent on excitation, while the PL decay times in the interlayers were shorter (e. g. 50 ps in sample E and

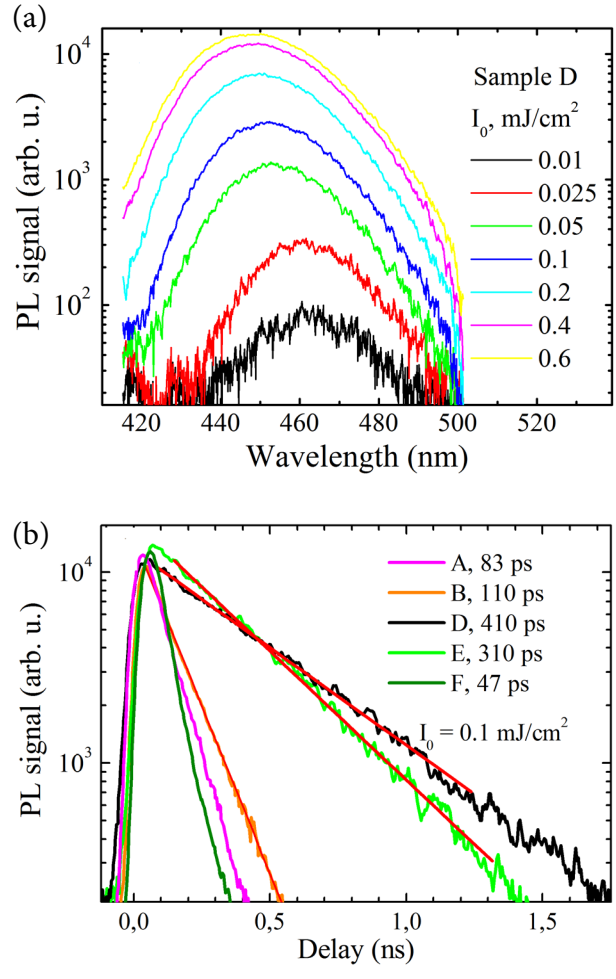

Fig. 11. (a) PL spectra in the triangular QWs at various excitations. (b) Comparison of PL decay kinetics of the QW emission in the samples. Excitation wavelength was set to 405 nm to avoid carrier excitation in the GaN buffer and barriers.

110 ps in sample B). Thus, a two times longer lifetime in sample B explained a two times stronger PL in it (see Fig. 10(b)).

3.4. DT spectra and LITG kinetics

In Fig. 12(a), a comparison between instantaneous DT and PL spectra is presented for sample D at selective photoexcitation. Within the entire spectral range the absorption decreases after the excitation (providing a negative DT signal) due to the state filling effect. Two distinct peaks in DT spectra are seen within the sub-nanosecond delay times range and are attributed, correspondingly, to absorption bleaching in the SEI interlayer (415 nm) and in the quantum wells (460 nm). The overlap of DT and PL spectra at the QW position indicates a strong photoexcitation absorption of QWs and, thus, sufficiently high density of states in quantum wells. During the first ~50 ps after the excitation, carrier transfer from higher to lower energy states occurs (compare the DT spectra at 0 ps and 50 ps in Fig. 12(a)). Later on, the DT signal decays due to carrier recombination; here, a shift of DT and PL spectra towards the longer wavelengths with time is attributed to rebuilding of initially screened polarization electric fields in QWs.

Figure 12(b) shows DT decay transients at various spectral positions within the PL band of QWs in sample D. Two decay components are present in these transients. The time decay constant of the faster component is shown in Fig. 12(c) (black squares online). It varies within 200–400 ps at given excitation and is close to the time constant of PL decay obtained from time-resolved PL measurements (red circles online in Fig. 12(c)). In addition, the spectral distributions of PL and DT decay times are very similar. This allows attributing this component to the radiative recombination of carriers that gives rise to photoluminescence. We note that PL time constant does not necessarily correspond to the radiative decay time, but is instead a result of radiative and nonradiative processes, $1/\tau_{PL} = 1/\tau_{rad} + 1/\tau_{nonrad}$. Therefore, the initial decay constants of DT and the PL decay time represent the fast nonradiative recombination time after the photoexcitation. At higher photoexcitations, PL decay time increases (see Fig. 12(c), red triangles online), as the nonradiative recombination centres are partially filled (a similar increase of the fast PL decay component was also observed in Ref. [7]). After carrier localization in the lowest energy states, the DT decay time becomes slower (note the second DT decay component with decay time constant well above 10 ns, Fig. 12(b)). We did not find a slow component in PL spectra and thus conclude that thermally activated carrier transfer from these

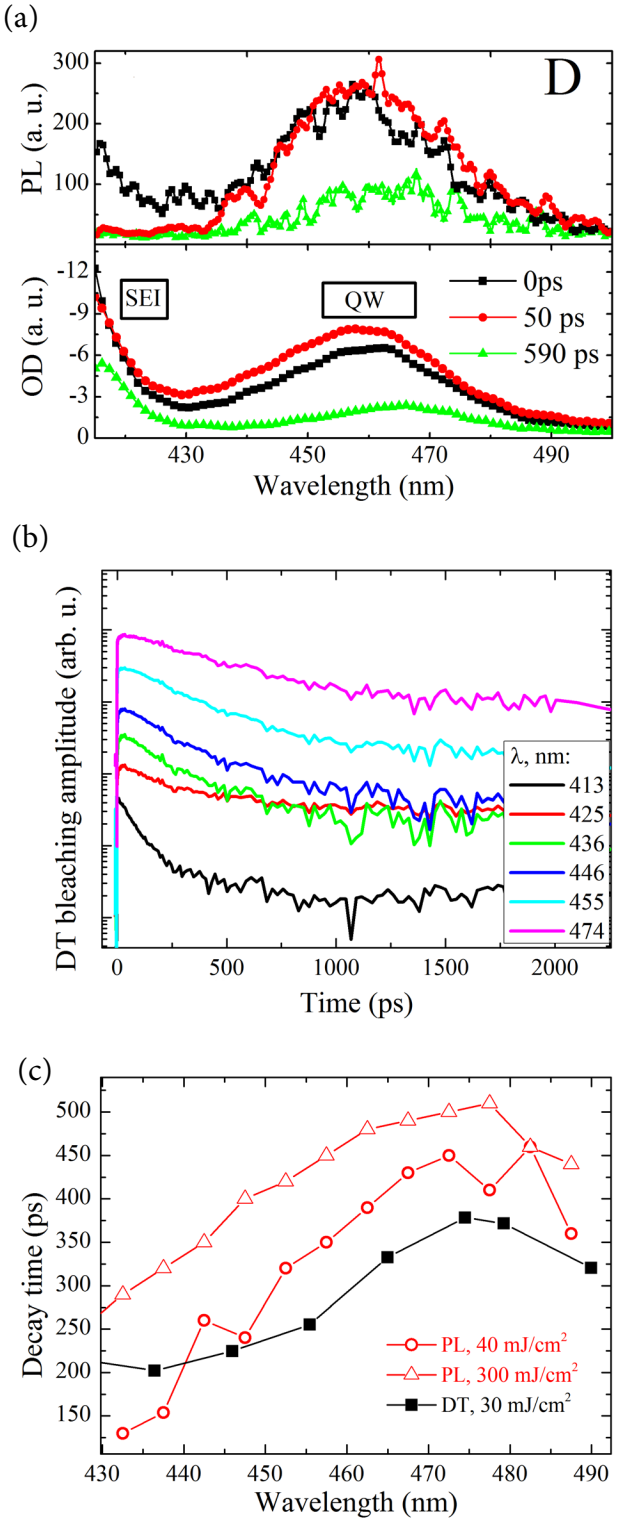

Fig. 12. Comparison of PL and DT data in sample D for a moderate excitation of 30–40 μJ/cm^2: (a) instantaneous PL and DT spectra of quantum wells at several delay times, (b) DT decay transients at various spectral positions (the transients are arbitrarily shifted with respect to each other for the sake of visibility), and (c) decay time constants of PL and DT signals against the spectral position.

localized states to nonradiative recombination centres is more efficient than the radiative recombination. We note that in less defective QWs the long lasting PL decay component is present [7]. As the long-decay DT signature is seen both in SEI and QWs (Fig. 12(b)), we attribute this component to nonradiative carrier recombination from deeply localized states, which are present both in the QW and SEI region. The DT decay time constants shorter than those of PL can be explained within the latter assumption since part of the carriers are being transferred to these immobile localized states.

The above-given PL and DT measurements pointed out that radiative processes were more efficient in the structures with non-rectangular-shape QWs. To compare the average carrier lifetime in differently shaped QWs, LITG measurements were performed at 387 nm excitation and 1030 nm probing. The pump wavelength was chosen to ensure photoexcitation of QWs and InGaN staircase and to avoid creation of excess carriers in the buffer GaN layer (selection of lower quantum energy would be preferable, but it provides less excess carriers and does not favour measurements in a wide dynamic range). Since LITG signal is proportional to the density of excited carriers integrated over the sample depth, the nonequilibrium carriers in the interlayer and in the QWs contribute to the measured diffraction signal. This approach allows evaluating the electronic quality of the grown structures at conditions similar to device performance at electrical carrier injection.

The kinetics of LITG decay for the differently shaped QWs are presented in Fig. 13 at low and high excitation energy densities. Here, the used low injection case was favourable to reveal processes of carrier transfer to localized states in QWs with the subsequent slower decay, while the high injection regime reveals the processes in higher energy states when the carriers are able to occupy the extended dates (in the given case, they may occupy the states in a wide SEI layer). In the structures D and E, the carrier lifetime peaks at ~300 ps, while in the structures A and B with standard well shape the carrier lifetime drops down to ~100 ps. At higher excitation, the lifetime in samples D and E also decreases to ~100 ps as the delocalized carriers occupy the extended states and face a higher number of fast nonradiative recombination centres. Therefore, carrier lifetime becomes similar to the one typical of the interlayer or the quantum well barriers.

The low-injection carrier lifetimes (~300 ps) coincide well with the PL decay times (300–400 ps in the QWs of D and E structures (Fig. 11(b)) and indicate the nonradiative recombination time in localized states. Despite that the average carrier lifetime of the heterostructure decreases with excitation, the PL decay time at the QW does not change significantly at even

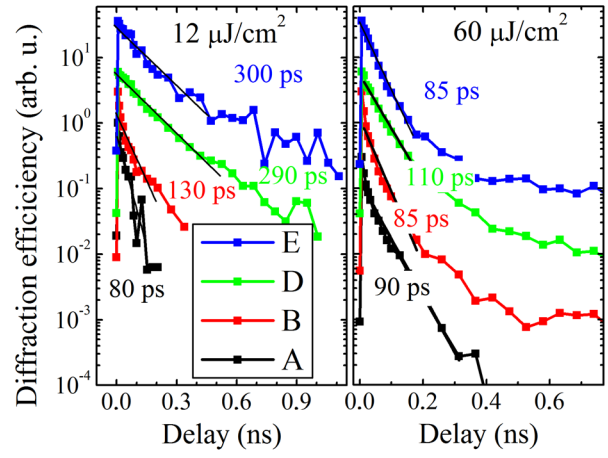

Fig. 13. LITG kinetics in differently shaped MQW structures at low and high excitation energy densities (grating period equals 7.27 μm). Kinetics are vertically displaced for clarity. The excitation quantum energy of 3.2 eV generates carriers in the entire heterostructure and monitors the spatially averaged carrier lifetime.

higher excitation which is a consequence of localized state saturation. This is an indication that localized state lifetime is weakly injection-dependent, i. e. the contribution of radiative emission with carrier density dependent recombination rate was not observed in the given set of samples.

4. Conclusions

Varying the growth regime, the active region of LED structure was modified by inserting a wide interlayer structure with gradual In concentration increase and subsequent growth of differently shaped InGaN quantum wells (rectangular, triangular, trapezoidal). Growth temperature variation allowed to obtain different In content in the quantum wells and formation of smooth quantum well barriers.

Measurements of photoluminescence spectra combined with the reactive-ion etching of the structure were applied for discrimination of PL signals originated in the InGaN interlayer structure, underlying quantum wells, and quantum barriers. Analysis of PL intensity dependence on excitation density provided technologically tailored conditions for enhanced carrier localization in the wells. The highest PL intensity was obtained in the heterostructure with triangularly shaped QWs.

Carrier dynamics was studied by TRPL, differential transmission, and light-induced transient grating techniques, providing carrier lifetimes, their spectral distribution, and revealing shorter carrier lifetime on the high-energy wing. Light-induced transient grating

technique was used to determine the average carrier lifetime in the entire heterostructure, in this way unravelling the electronic quality of the internal LED structure at conditions similar to device performance. Grating decay rates at low and high excitation energy densities revealed increasing with photoexcitation nonradiative recombination rate in the triangular and trapezoidal wells. This study proved that the implemented strain management led to the lower dislocation density, smoother surface, longer localized carrier lifetime, and eventually the highest PL intensity in the triangularly shaped quantum wells.

Acknowledgement

The authors acknowledge support of the European Social Fund under Project VP1-3.1-ŠMM-07K-02-006.

References

[1] G. Verzellesi, D. Saguatti, M. Meneghini, F. Bertazzi, M. Goano, G. Meneghesso, and E. Zanoni, Efficiency droop in InGaN/GaN blue light-emitting diodes: Physical mechanisms and remedies, J. Appl. Phys. **114**, 071101 (2013).

[2] V. Avrutin, S.A. Hafiz, F. Zhang, Ü. Özgür, H. Morkoç, and A. Matulionis, InGaN light-emitting diodes: Efficiency-limiting processes at high injection, J. Vac. Sci. Technol. A **31**, 050809 (2013).

[3] J. Piprek, Efficiency droop in nitride-based light-emitting diodes, Phys. Status Solidi A **207**, 2217–2225 (2010).

[4] E. Kioupiakis, P. Rinke, K.T. Delaney, and C.G. Van de Walle, Indirect Auger recombination as a cause of efficiency droop in nitride light-emitting diodes, Appl. Phys. Lett. **98**, 161107 (2011).

[5] J. Hader, J.V. Moloney, and S.W. Koch, Density-activated defect recombination as a possible explanation for the efficiency droop in GaN-based diodes, Appl. Phys. Lett. **96**, 221106 (2010).

[6] T. Malinauskas, A. Kadys, T. Grinys, S. Nargelas, R. Aleksiejūnas, S. Miasojedovas, J. Mickevičius, R. Tomašiūnas, K. Jarašiūnas, M. Vengris, S. Okur, V. Avrutin, X. Li, F. Zhang, Ü. Özgür, and H. Morkoç, Impact of carrier localization, recombination, and diffusivity on excited state dynamics in InGaN/GaN quantum wells, Proc. SPIE **8262**, 82621S-1 (2012).

[7] R. Aleksiejūnas, K. Gelžinytė, S. Nargelas, K. Jarašiūnas, M. Vengris, E.A. Armour, D.P. Byrnes, R.A. Arif, S.M. Lee, and G.D. Papasouliotis, Diffusion-driven and excitation-dependent recombination rate in blue InGaN/GaN quantum well structures, Appl. Phys. Lett. **104**, 022114 (2014).

[8] J.I. Shim, H. Kim, D.S. Shin, and H.Y. Yoo, An explanation of efficiency droop in InGaN-based light emitting diodes: saturated radiative recombination rate at randomly distributed In-rich active areas, J. Korean Phys. Soc. **58**, 503–508 (2011).

[9] B.-J. Ahn, T.-S. Kim, Y. Dong, M.-T. Hong, J.-H. Song, J.-H. Song, H.-K. Yuh, S.-C. Choi, D.-K. Bae, and Y. Moon, Experimental determination of current spill-over and its effect on the efficiency droop in InGaN/GaN blue-light-emitting diodes, Appl. Phys. Lett. **100**, 031905 (2012).

[10] X. Ni, X. Li, J. Lee, S. Liu, V. Avrutin, Ü. Özgür, H. Morkoç, A. Matulionis, T. Paskova, G. Mulholland, and K.R. Evans, InGaN staircase electron injector for reduction of electron overflow in InGaN light emitting diodes, Appl. Phys. Lett. **97**, 031110 (2010).

[11] M.H. Kim, M.F. Schubert, Q. Dai, J.K. Kim, E.F. Schubert, J. Piprek, and Y. Park, Origin of efficiency droop in GaN-based light-emitting diodes, Appl. Phys. Lett. **91**, 183507 (2007).

[12] S.-H. Han, D.-Y. Lee, H.-W. Shim, G.-Ch. Kim, Y.S. Kim, S.-T. Kim, S.-J. Lee, Ch.-Y. Cho, and S.-J. Park, Improvement of efficiency droop in InGaN/GaN multiple quantum well light-emitting diodes with trapezoidal wells, J. Phys. Appl. Phys. **43**, 354004 (2010).

[13] H. Zhao, G. Liu, J. Zhang, J.D. Poplawsky, V. Dierolf, and N. Tansu, Approaches for high internal quantum efficiency green InGaN light-emitting diodes with large overlap quantum wells, Opt. Express **19**, A991–A1007 (2011).

[14] M. Leyer, J. Stellmach, Ch. Meissner, M. Pristovsek, and M. Kneissl, The critical thickness of InGaN on (0001) GaN, J. Cryst. Growth **310**, 4913–4915 (2008).

[15] K. Pantzas, G. Patriarche, G. Orsal, S. Gautier, T. Moudakir, M. Abid, V. Gorge, Z. Djebbour, P.L. Voss, and A. Ougazzaden, Investigation of a relaxation mechanism specific to InGaN for improved MOVPE growth of nitride solar cell materials, Phys. Status Solidi A **209**(1), 25–28 (2012).

[16] K. Jarašiūnas, R. Aleksiejūnas, T. Malinauskas, V. Gudelis, T. Tamulevičius, S. Tamulevičius, A. Guobienė, A. Usikov, V. Dmitriev, and H.J. Gerritsen, Implementation of diffractive optical element in four-wave mixing scheme for *ex situ* characterization of hydride vapor phase epitaxy-grown GaN layers, Rev. Sci. Instrum. **78**, 033901 (2007).

[17] P. Ščajev, K. Jarašiūnas, S. Okur, Ü. Özgür, and H. Morkoç, Carrier dynamics in bulk GaN, J. Appl. Phys. **111**, 023702 (2012).

[18] P. Ščajev, A. Usikov, V. Soukhoveev, R. Aleksiejūnas, and K. Jarašiūnas, Diffusion-limited nonradiative recombination at extended defects in hydride vapor phase epitaxy GaN layers, Appl. Phys. Lett. **98**, 202105 (2011).

[19] G. Li, S.J. Chua, S.J. Xu, W. Wang, P. Li, B. Beaumont, and P. Gibart, Nature and elimination of yellow-band luminescence and donor–acceptor emission of undoped GaN, Appl. Phys. Lett. **74**, 2821–2823 (1999).

[20] V.Yu. Davydov, A.A. Klochikhin, V.V. Emtsev, D.A. Kurdyukov, S.V. Ivanov, V.A. Vekshin, F. Bechstedt, J. Furthmüller, J. Aderhold, J. Graul, A.V. Mudryi, H. Harima, A. Hashimoto, A. Yamamoto, and E.E. Haller, Band gap of hexagonal InN and InGaN alloys, Phys. Status Solidi B **234**(3), 787–795 (2002).

[21] N. Peyghambarian, S.W. Koch, and A. Mysyrowicz, *Introduction to Semiconductor Optics* (Prentice Hall, 1993).

FOTOLIUMINESCENCIJOS YPATUMAI IR KRŪVININKŲ DINAMIKA InGaN HETEROSANDAROSE SU PLAČIU LAIPTUOTU TARPSLUOKSNIU IR SKIRTINGO PROFILIO KVANTINĖMIS DUOBĖMIS

A. Kadys, T. Malinauskas, M. Dmukauskas, I. Reklaitis, K. Nomeika, V. Gudelis, R. Aleksiejūnas, P. Ščajev, S. Nargelas, S. Miasojedovas, K. Jarašiūnas

Vilniaus universiteto Taikomųjų mokslų institutas, Vilnius, Lietuva

Santrauka

Pristatome išsamius fotosužadintų krūvininkų dinamikos tyrimus daugialypėse InGaN kvantinėse sandarose su plačiu laiptuotu tarpsluoksniu ir skirtingo profilio kvantinėmis duobėmis (stačiakampėmis, trikampėmis, trapecinėmis). Šis įtempimų valdymo būdas dėl palaipsniui didėjančio In kiekio tarpsluoksnyje ir sklandaus sandūrų tarp kvantinių duobių bei barjerų formavimo leido sumažinti dislokacijų tankį. Daugialypės kvantinės sandaros, orientuotos išilgai c ašies ir šviečiančios ties 470 nm, buvo pagamintos Vilniaus universiteto Taikomųjų mokslų instituto MOCVD reaktoriuje. Fotoliuminescencijos (FL) spektrų matavimai buvo atlikti nuolatinės veikos ir impulsinio žadinimo sąlygomis. Bandinių reaktyvus joninis ėsdinimas leido identifikuoti FL atsaką iš InGaN tarpsluoksnio, kvantinių duobių ir kvantinių barjerų, tokiu būdu parodant su auginimu susijusias sąlygas, lemiančias geresnę krūvininkų lokalizaciją duobėse. Iš laikinės skyros FL ir skirtuminio pralaidumo kinetikų įvertintos krūvininkų gyvavimo trukmės (ir jų spektrinis pasiskirstymas) buvo ilgiausios trikampėse kvantinėse duobėse, kuriose taip pat stebėtas didžiausias FL intensyvumas. Šviesa indukuotų difrakcinių gardelių metodika panaudota nustatant erdviškai suvidurkintą krūvininkų gyvavimo trukmę visoje heterostruktūroje, tai leido įvertinti vidinės šviestuko struktūros kokybę panašiomis prietaisų veiklai sąlygomis. Gardelių irimo spartos esant žemam ir aukštam žadinimo energijos tankiui atskleidė su fotosužadinimu augančią nespindulinės rekombinacijos spartą trikampio ir trapecinio profilio duobėse.